



Article

Analysis of Ionospheric Disturbances during X-Class Solar Flares (2021–2022) Using GNSS Data and Wavelet Analysis

Charbeth López-Urías ^{1,*} , G. Esteban Vazquez-Becerra ¹ , Karan Nayak ¹ and Rebeca López-Montes ²

¹ Department of Earth and Space Sciences, Autonomous University of Sinaloa, Culiacán 80040, Mexico; gvazquez@uas.edu.mx (G.E.V.-B.); nayakkaran.facite@uas.edu.mx (K.N.)

² Department of Applied Geophysics, Center for Scientific Research and Higher Education of Ensenada, La Paz 23050, Mexico; rebecamont@gmail.com

* Correspondence: charbethlopez@uas.edu.mx; Tel.: +52-6672-433-822

Abstract: The influence of solar activity on the ionosphere, a critical area of investigation due to its relevance to the Sun–Earth relationship, has been extensively examined through various methodologies. The ability of solar events to induce disturbances in both the ionosphere and the geomagnetic field is widely acknowledged. This specific study focused on sporadic incidents resulting from X-class solar flares that occurred between 2021 and 2022. Utilizing a methodology that involved analyzing data at 5Hz intervals using wavelet algorithms, the data from the GNSS stations of the National Autonomous University of Mexico (UNAM) were investigated. The primary emphasis was on deducing the Total Electron Content (TEC) within the ionosphere. Subsequently, this parameter for each satellite during instances of solar flares was analyzed. The approach uncovered disruptions in the ionosphere triggered by solar flares, even in cases where events transpired at the periphery of the solar disk and were of magnitudes smaller than X2.

Keywords: ionosphere; GNSS; wavelets; solar flare; total electron content



Citation: López-Urías, C.; Vazquez-Becerra, G.E.; Nayak, K.; López-Montes, R. Analysis of Ionospheric Disturbances during X-Class Solar Flares (2021–2022) Using GNSS Data and Wavelet Analysis. *Remote Sens.* **2023**, *15*, 4626. <https://doi.org/10.3390/rs15184626>

Academic Editor: Yunbin Yuan and Angela Aragón-Ángel

Received: 22 August 2023

Revised: 19 September 2023

Accepted: 19 September 2023

Published: 20 September 2023



Copyright: © 2023 by the authors. Licensee MDPI, Basel, Switzerland. This article is an open access article distributed under the terms and conditions of the Creative Commons Attribution (CC BY) license (<https://creativecommons.org/licenses/by/4.0/>).

1. Introduction

The ionosphere, situated in the upper region of Earth’s atmosphere, maintains a continuous state of ionization primarily caused by solar radiation. This layer spans from approximately 60 km to 1000 km above the Earth’s surface [1]. The Earth’s ionosphere plays a crucial role in facilitating high-frequency communication and navigation systems, serving as a critical medium for the propagation of radio waves. It exhibits complicated spatial and temporal changes that can disrupt the transmission of radio signals, adversely impacting satellites, communication, navigation, and geographic location [2–6]. The ionosphere’s Total Electron Content (TEC) is a key parameter that characterizes the integrated electron density along the signal’s path. The TEC is the total number of electrons in the path from the satellite to the receiver, in a column with a 1 m² cross-section. Its unit is the TECU, where 1TECU = 10¹⁶ e/m⁻² is a parameter that describes the behavior of the ionosphere [7]. During radio wave propagation, the electron density in the Earth’s atmosphere is expected to vary over a nominal range of 10¹⁶ e/m⁻² to 10¹⁹ e/m⁻², being the minimum and maximum values reached around midnight and mid-afternoon, respectively [8], and is obtained from the signals L1 (1.57542 GHz) and L2 (1.2276 GHz) of the Global Positioning Systems [9]. However, this region is not impervious to the influence of solar activity, particularly solar flares—intense bursts of radiation and energy released from the Sun’s surface. Solar flares can lead to significant disturbances in the ionosphere, impacting TEC and affecting the reliability and performance of high-frequency communication and navigation systems.

A solar flare, also referred to as a chromospheric burst, is a significant release of high-energy radiation frequently observed from the Sun. It holds immense importance in the realm of space weather due to its powerful and energetic nature [10,11]. Solar

flares stem from the active region of the Sun, typically near a cluster of sunspots, and can endure anywhere from minutes to hours. These solar flares represent the most powerful and abrupt explosive events during which a substantial number of high-energy protons, electrons, and intense radiation spanning the entire electromagnetic spectrum are emitted. Consequently, there is a notable surge in extreme ultraviolet (EUV) and X-ray emissions, leading to additional ionization in the dayside ionosphere [12].

Numerous studies have indicated a complex relationship between solar flares and ionospheric perturbations, with the potential to cause disruptions in TEC. Variations in electron density during solar flares can affect the phase and amplitude of radio signals propagating through the ionosphere, leading to signal fading, scintillation, and navigation inaccuracies [13–17]. Such effects can have substantial consequences for global navigation satellite systems (GNSS), satellite-based communication links, and other applications that rely on ionospheric propagation. Yasyukevich et al. [13] investigated the influence of X-class solar flares on GNSS signals during the solar maximum of Cycle 24. Their study utilized GNSS data to analyze the TEC variations caused by solar flares and assess the impact on positioning accuracy. Sreeja [14] reviewed the space weather effects on high-accuracy GNSS-based navigation, discussing the implications of solar flares on GNSS signal propagation, TEC estimation, and navigation performance. Yadav et al. [15] analyzed the impacts of the St. Patrick's Day storm on the high-latitude ionosphere using GPS and CHAMP data. Their study investigated the TEC variations induced by solar flares during this geomagnetic storm. Reddybattula et al. [16] examined the ionospheric response to the solar flare of 10 September 2017 and its impact on GNSS positioning in the Asia–Oceania region. Their research highlighted the regional variability of TEC disturbances caused by solar flares. Currently, much research is being carried out using GPS technology, because the impact of the ionosphere on GPS signals provides the information necessary to understand how the ionosphere varies temporally and spatially, and how this affects navigation and navigation. satellite communication systems [18].

This study investigates the noteworthy influence of solar flares on TEC at high frequencies, with a focus on their subsequent implications for space weather. Solar flares, powerful bursts of high-energy radiation emitted by the Sun, have been recognized as influential space weather events that disrupt the ionosphere's electron density and cause variations in TEC. This research methodically analyzes data from multiple Global Navigation Satellite System (GNSS) stations during various solar flare events. By applying wavelet analysis and careful consideration of sampling intervals, this study establishes the optimal conditions for detecting and characterizing ionospheric disturbances induced by solar flares. This research not only highlights the complex interplay between solar flares and the ionosphere but also establishes a robust methodology for identifying and analyzing these disturbances, contributing to our understanding of space weather impact on Earth's technological infrastructure.

2. Data and Methods

2.1. TEC Data

GNSS systems utilize two or three frequencies to assess the characteristics of the ionosphere. These frequencies aid in the assessment of the ionosphere itself rather than its influence on the signals. Having access to dual frequencies allows for a more accurate examination of relative phase delays between signals, such as L1 and L2. A greater electron density in the ionosphere results in a more pronounced difference between the signals, as the impact of density on signals varies depending on their frequency [19]. Signals are affected by the ionosphere in terms of both amplitude and phase [20]. The extent of the dispersive effect is directly proportional to the total electron content [21].

In the conducted study, data from six GNSS stations affiliated with the Institute of Geophysics at the National Autonomous University of Mexico were utilized (see Table 1). The RINEX files were processed to exclusively retain the necessary parameters for the calculation of Total Electron Content (TEC). For slant TEC, particularly in the case of TEC

calculated from pseudorange, Equation (1) [22] was employed, characterized by noise yet maintaining ambiguity-free characteristics [23]. To derive phase-based TEC, Equation (2) was applied, yielding results with less noise albeit being ambiguous.

$$TEC_R = 9.52(R_1 - R_2) \quad (1)$$

$$TEC_\Phi = 9.52(\lambda_1 \cdot \Phi_1 - \lambda_2 \cdot \Phi_2) \quad (2)$$

The values of slant TEC depend on the satellite's elevation angle, making it necessary to compute the vertical TEC. The vertical TEC is obtained using the mapping function (Equation (3)), which assumes an ionospheric point of interest at a height of 350 km [24].

$$VTEC = STEC \cdot \cos \left[\arcsin \frac{R_e \cos(\theta)}{R_e + h} \right] \quad (3)$$

Here, R_e represents the radius of the Earth (6371.2 km), h represents the height of the ionosphere relative to the Earth's surface (350 km), and θ denotes the elevation angle between the satellite and the receiver, measured in degrees.

Table 1. GNSS station coordinates.

Station	Latitude (N)	Longitude (W)	Height (m)
SPIG	31°02'45.87"	115°27'57.68"	2751.110
UCOE	19°48'47.47"	101°41'39.86"	1977.427
UNPM	20°52'06.66"	86°52'05.43"	1.800
OXUM	15°39'44.09"	96°29'56.50"	82.267
SSNX	19°19'37.78"	99°10'36.37"	2275.850
UTEO	19°44'28.46"	99°11'19.00"	2267.452

2.2. Wavelets

The Discrete Wavelet Transform (DWT) is a method that iteratively decomposes an input signal, $S_0(n)$, into two lower resolution subsequences, known as approximation and detail. The subsequences $S_i(n)$ and $W_i(n)$ represent the approximation and detail, respectively, of the signal at level i [25]. The calculation of the approximation of the signal at level $i + 1$ is performed according to Equations (4) and (5).

$$S_{i+1}(n) = \sum_k g(k)S_i(2n - k) \quad (4)$$

The detail of the signal at level $i + 1$ can be calculated as follows:

$$W_{i+1}(n) = \sum_k h(k)S_i(2n - k) \quad (5)$$

This calculation process, known as the Mallat pyramid algorithm [26], is employed for the DWT.

According to Osorio et al. [27], in certain cases, it is advantageous to limit the amount of data for signal processing involving wavelet coefficients. Consequently, the number of analyzed samples is reduced by half through compression. In our scenario, even though we had time windows ranging from 2 to 4 h, it was feasible to detect ionospheric disturbances using wavelets at levels 7 and 8, where levels 7 and 8 are the seventh and eighth application of the wavelet algorithms, respectively. Figure 1 displays the results of the wavelet analysis for one of the satellites, where it can be observed that levels 7 and 8 exhibit a noticeable disturbance at the time of the event. In addition to this, we calculated the correlation between each of the levels and TEC, aiming to have a more solid foundation for selecting the wavelet levels to use. This led to the conclusion that the best levels are 7 and 8. It is worth mentioning that the application of each wavelet level is similar to applying

filtering for high and low frequencies, with one being implemented for detail and the other for approximation.

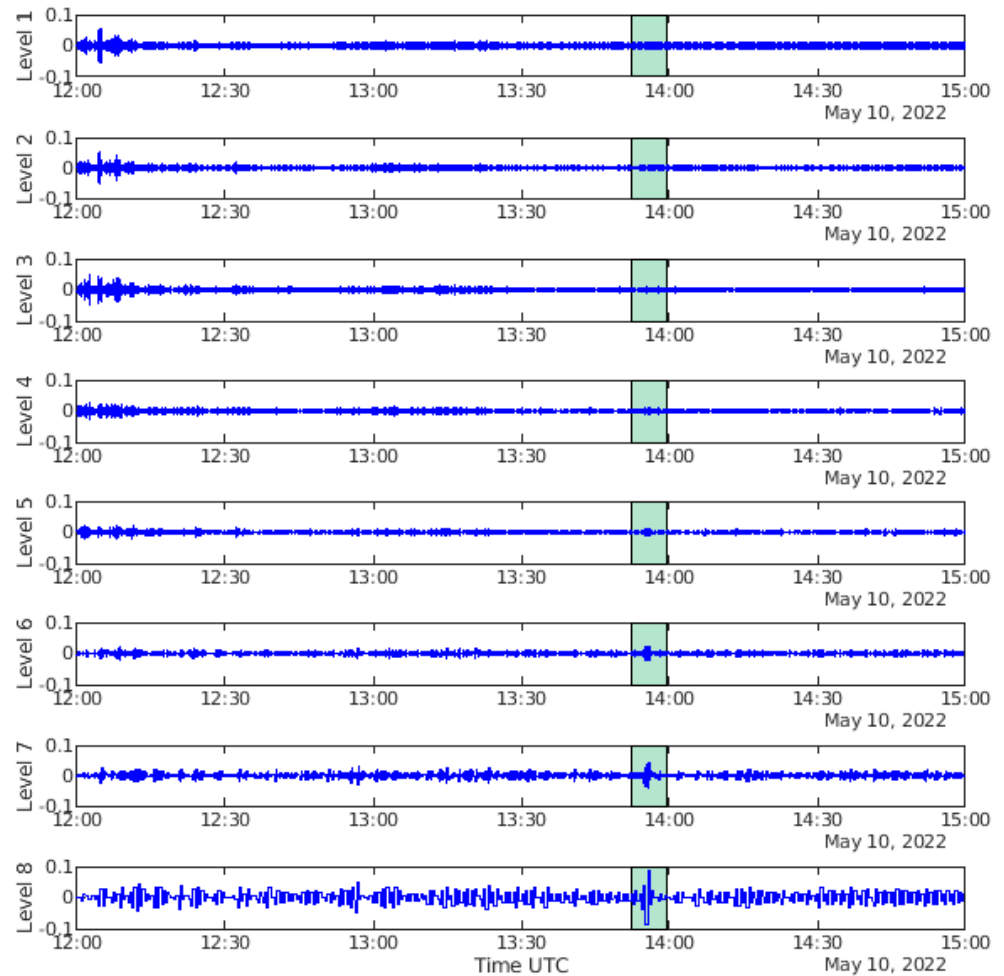


Figure 1. The figure illustrates the differentiation of each level's application from 1 to 8 in wavelet algorithms used for solar flare detection. The green rectangle is the solar flare being more distinct in level 7 and 8.

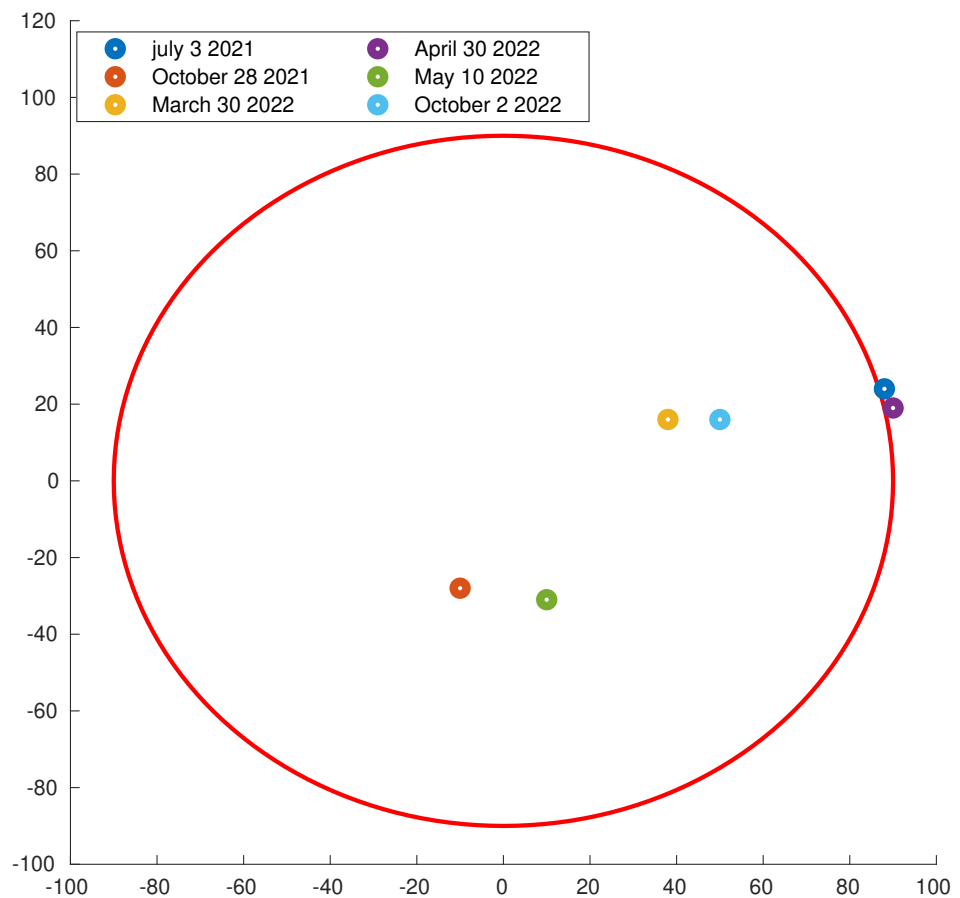
2.3. Analysis Methods

For over thirty years, the Geostationary Operational Environmental Satellite (GOES) series from the National Oceanic and Atmospheric Administration (NOAA) has been responsible for measuring meteorological and space weather phenomena. One of the essential components of the GOES-R instrument suite is the EUV and X-Ray Irradiance Sensor System (EXIS), which consists of two instruments designed to monitor solar spectral irradiance: the Extreme Ultraviolet Sensor (EUVS) and the X-Ray Sensor (XRS) [28]. For our study, we utilize data from the GOES 17 satellite to select and analyze six solar flare events that occurred during the years 2021 and 2022 (details provided in Table 2).

Figure 2 displays the positions of these solar flares on the solar disk, revealing occurrences both in the central region and at the periphery. Recognizing the spatial distribution of these solar eruptions is crucial as it offers pivotal insights into solar activity dynamics. Additionally, it is important to note that, in accordance with the Dst index (Figure 3), the Earth's magnetic field remained calm during this period. This calm magnetic field condition stands as an essential factor for our study, as it ensures that disturbances arising from magnetic field fluctuations are minimal. The data used from the dst index were obtained from the Center for Geomagnetism and Space Magnetism Data Analysis at Kyoto University.

Table 2. Event Features.

Date	Day GPS	Start Time (UT)	Peak Time (UT)	End Time (UT)	Flare Class
03 July 2021	184	14:18	14:29	14:34	X1.5
28 October 2021	301	15:17	15:35	15:48	X1
30 March 2022	89	17:21	17:37	17:46	X1.3
30 April 2022	120	13:37	13:47	13:52	X1.1
10 May 2022	130	13:50	13:55	13:59	X1.5
2 October 2022	275	19:53	20:25	20:34	X1.0

**Figure 2.** Location of the solar flare on the solar disk.

When investigating the Total Electron Content (TEC) on a per-station basis, we risk overlooking significant insights offered by analyzing TEC data for individual satellites. The computation of TEC for each station mandates the application of diverse filters to counter temporal mean effects that arise as the number of visible satellites observed by the station fluctuates. By individually scrutinizing TEC for each satellite, a more intricate evaluation of TEC conditions becomes achievable. To further enhance our understanding of ionospheric perturbations, we calculated TEC at 5 Hz intervals, allowing us to capture ionospheric fluctuations every 1/5 of a second.

The deployment of multiple monitoring stations played a pivotal role in mitigating distortions arising solely from the peculiarities of a single station's receiver. Employing wavelet analysis for TEC examination enabled us to distinctly and concisely pinpoint the influence of solar flares on TEC while simultaneously highlighting distinct frequency components evident over time.

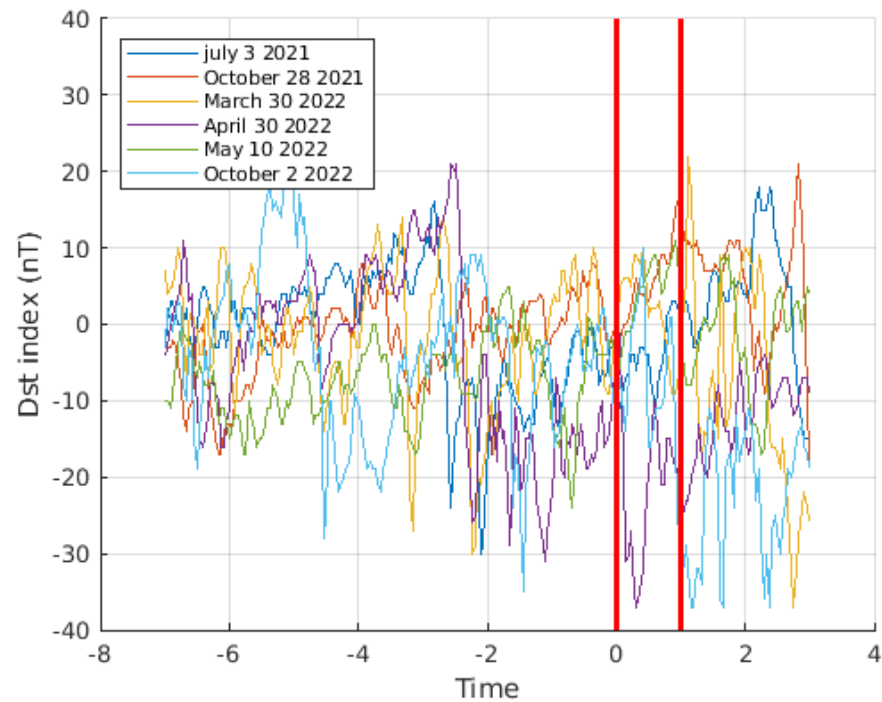


Figure 3. Variations of the Dst index during the events.

3. Results and Discussion

3.1. Event 1 (3 July 2021)

The event on 3 July 2021 took place in region AR12838, located in zone N24 W88, reaching a higher intensity in the X1.59 type flare, starting at 14:18 UTC and reaching its maximum intensity at 14:29 UTC, ending at 14:34 UTC. Although the event occurred in a location that was not favorable for its study, alterations in the ionosphere can still be found due to the implemented methodology. During the event time period, we have information from six GNSS stations (UTEQ, UNPM, OXUM, SPIG, SSNX and UCOE), with an average of five satellites' information for each station during the event hour, with a window from 13:00 UTC to 15:00 UTC. Figure 4 shows the results of the event for only OXPE station (PRN 14), including X-ray irradiance measurements, $vTEC$, and wavelet details at different levels over a 2-hour period in UTC time. On the other hand, Figure 5 shows the wavelet results for the same event utilizing all six stations. In these, it is possible to identify the event in question; however, at the SSNX station, despite identifying the event, there are signal alterations that are not shown in other receivers, even though they interact with the same satellites. Therefore, for this station, it could be said that this is due to disturbances independent of the solar flare, or even noise from the receiver. Satellite 30 presented alterations at the beginning of the time window for all receivers; nevertheless, it is possible to identify the alterations that occurred due to the solar flare. Satellites 15 and 19 of the SPIG station had a poorer response, making it difficult to clearly identify the event. A possible cause of this could be the location of the station, which is further north than the other stations studied.

The solar flare occurred on 3 July 2021, but according to the magnetic field and GOES 17 satellite data, the previous day (2 July 2021) was calm (without external disturbances in the ionosphere). Therefore, for comparative purposes, we applied the same algorithms to this quiet day, yielding random and nonsensical alterations as results. This is in contrast to when a solar flare occurs, resulting in disturbances across all stations at a specific time (during the solar flare event). For each of the events, we followed the same procedure, generating a graph for a calm day and another for the event day. In the case of Event 1, Figure 6 presents the obtained results.

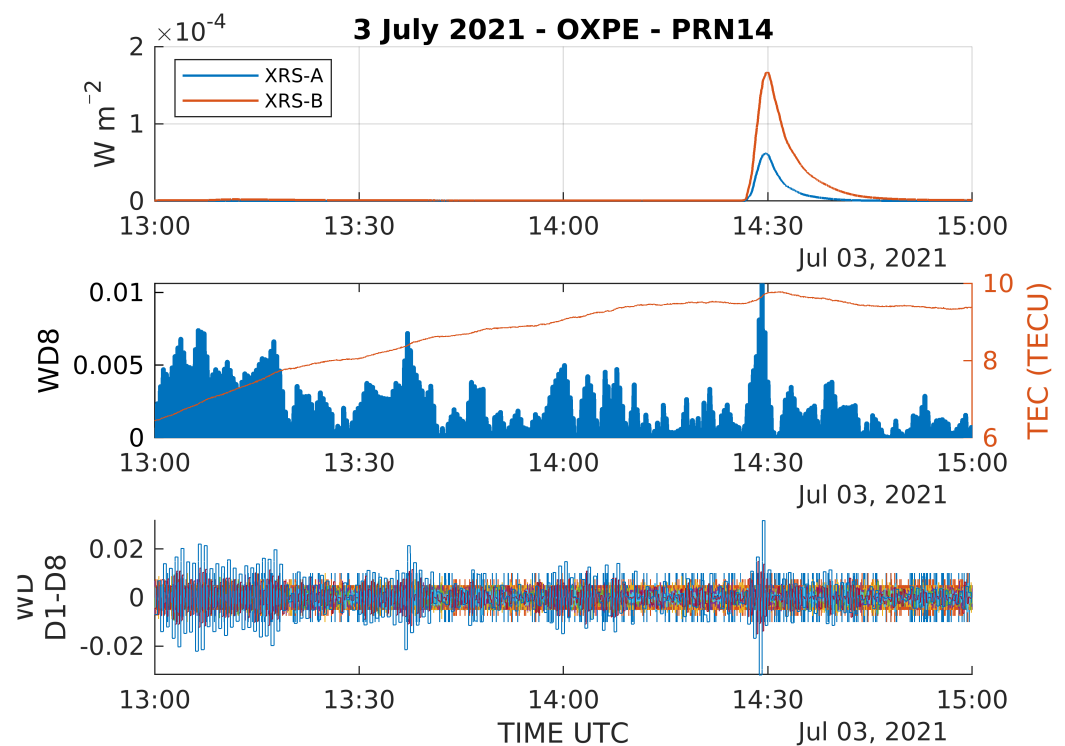


Figure 4. Results from the X1.59 solar flare event that occurred on 3 July 2021, in Region AR12838 (Zone N24 W88) for the OXPE station (PRN 14). The upper graph shows two irradiance measurements within the X-ray part of the electromagnetic spectrum, which were obtained through solar observations. These measurements originate from the XRS-A and XRS-B channels. The XRS-A channels detect wavelengths ranging from 0.05 to 0.4 nm, represented by the solid blue line, while the XRS-B channels cover wavelengths from 0.1 to 0.8 nm, represented by the solid red line. In the middle graph, the vTEC (vertical total electron content) is depicted as a solid red line measured in TECU, and it is accompanied by wavelet details at level 8 (WD8), represented by blue column bars. The last graph displays the wavelet details at all levels (WD D1-D8) together. The X-axis represents the time in UTC for a 2-hour period, with each grid corresponding to 30 min.

3.2. Event 2 (28 October 2021)

On 28 October 2021, there were two intense solar flares observed. One of these flares was categorized as type M with an intensity level of M8.77, while the other was of type X with an intensity of X1.06. The M-type flare was observed during the nighttime hours. As a result, the focus of the study is directed towards the X-type flare, which attained its peak intensity at 15:35 UTC. The initiation of this flare took place at 15:17 UTC, and its conclusion was marked at 15:48 UTC. The origin of this X-type flare was traced back to the solar region known as AR12887, situated at coordinates S28 E10.

The impact of this event was visible at the three designated stations, namely, UNPM, SPIG, and UCOE. These stations encountered notable disturbances during the time of the flare. It is worth noting that Satellite 24 displayed an unusual noise pattern at 17:48 UTC. This occurrence is potentially linked to noise originating from the mentioned satellite, especially considering the considerable geographical separation between the stations where the noise was detected.

Event 2 exhibited comparable features to the previous one, even though, in this instance, we had fewer satellites accessible across all stations. Nonetheless, a pronounced disturbance was evident, coinciding with the solar flare's occurrence. However, during the calm day, the alterations appeared random, lacking a consistent pattern attributable to flare-induced disruptions (Figure 7).



Figure 5. The wavelet results for the same event with accordance to all the six stations (OXPE, SPIG, SSNX, UCOE, UNPM, UTEO), each with three PRNs. The specific details for each station align with those depicted in Figure 4.

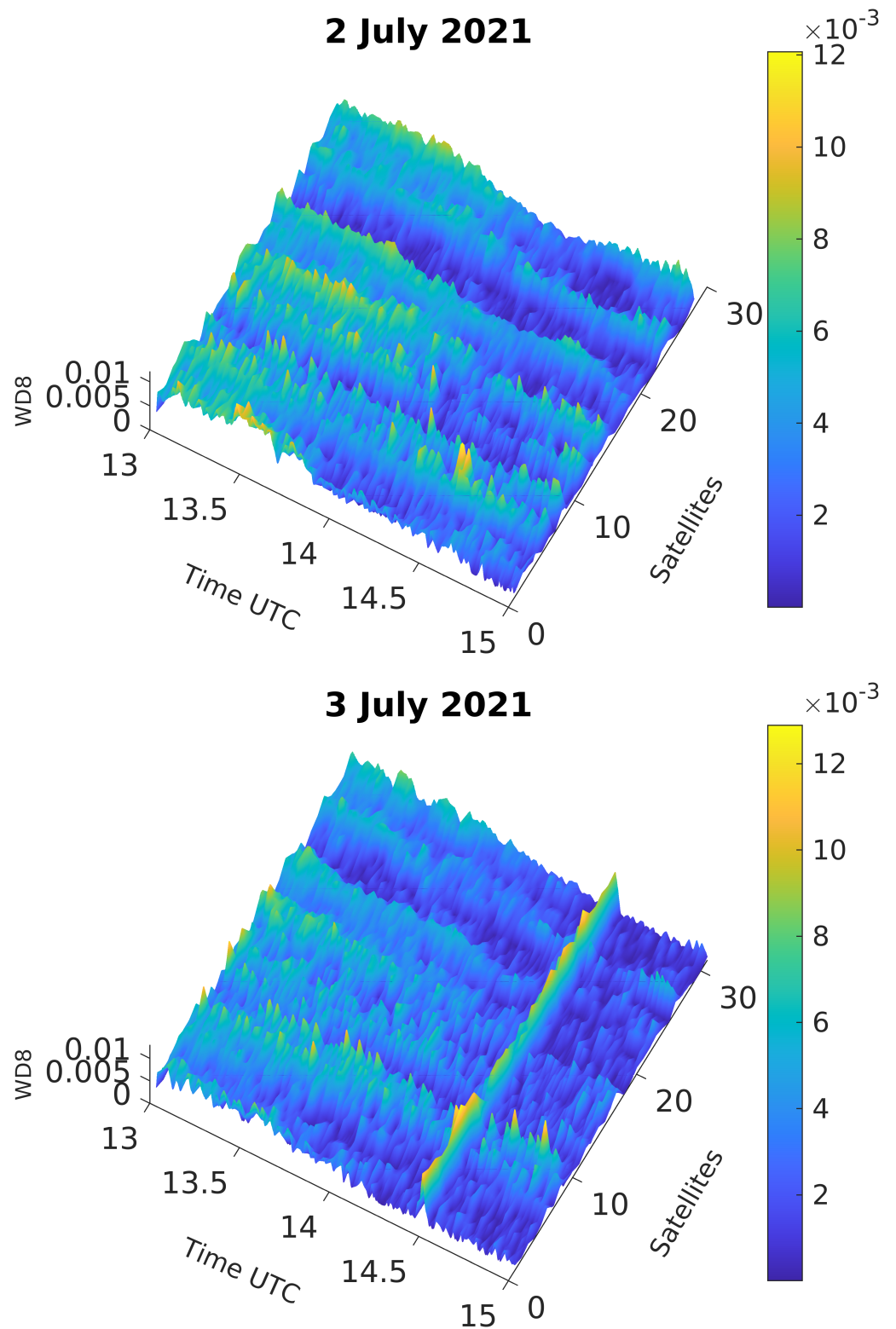


Figure 6. Visualization of Total Electron Content Wavelet Analysis from GNSS Signals for the Event on 3 July 2021

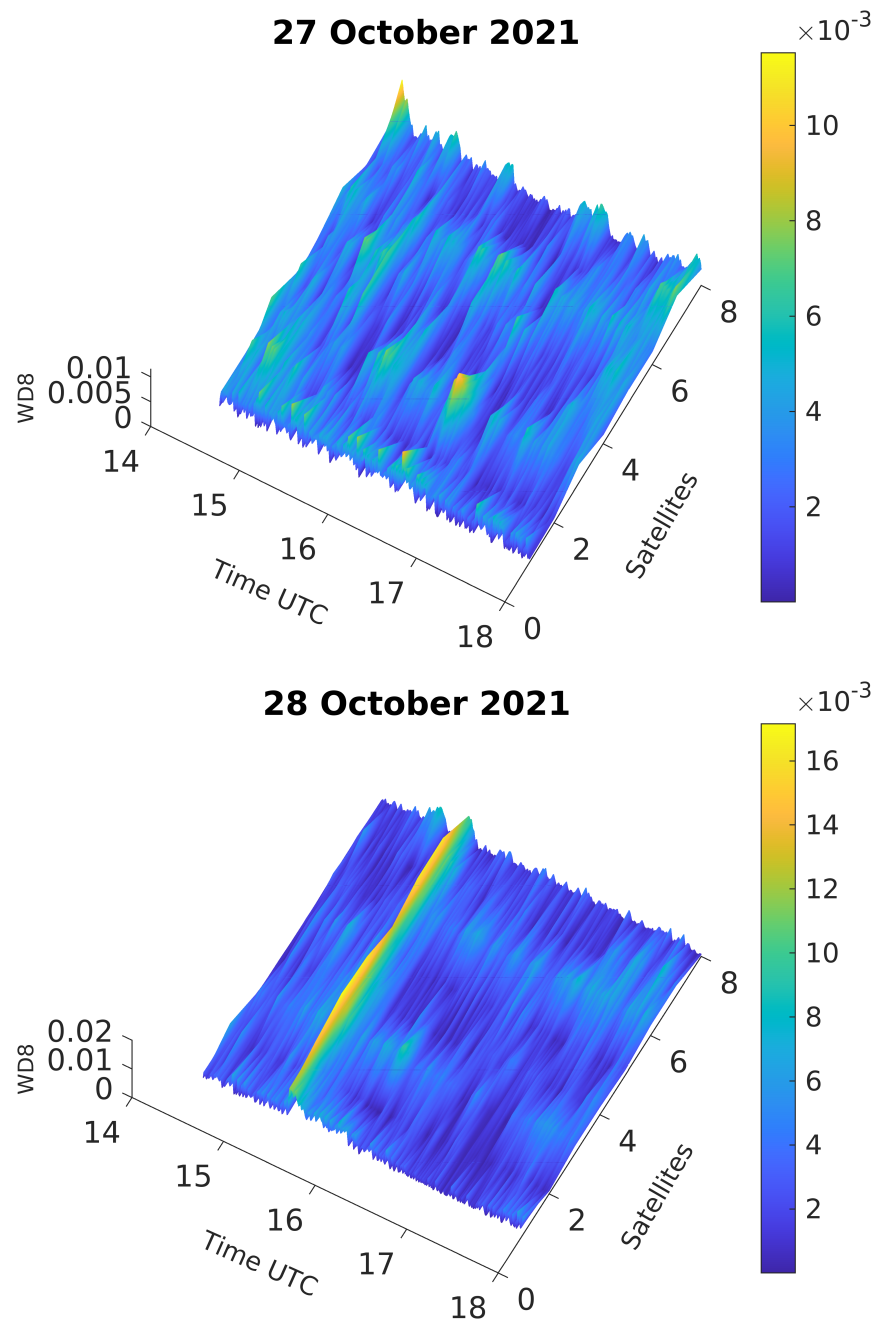


Figure 7. Visualization of Total Electron Content Wavelet Analysis from GNSS Signals for the Event on 28 October 2021.

3.3. Event 3 (30 March 2022)

On 30 March 2022, the Sun emitted a solar flare in the AR12975 region, which reached an X1.38 type intensity. This flare originated at location N16 W38, starting at 17:21 UTC, reaching its maximum intensity at 17:37 UTC, and ending at 17:46 UTC. This event caused disturbances in the ionosphere that were visible at all analyzed stations (UNPM, OXUM, SPIG, SSNX, and UCOE). In addition, for satellites 7 and 30, signal noise increased after the event.

In this instance, the alterations were also noticeable, although not as pronounced as the previous ones. Nonetheless, it remains possible to identify the moment of the solar flare. The results from the calm day display alterations that would not be associated with the flare but rather with the daily ionospheric cycle (Figure 8).

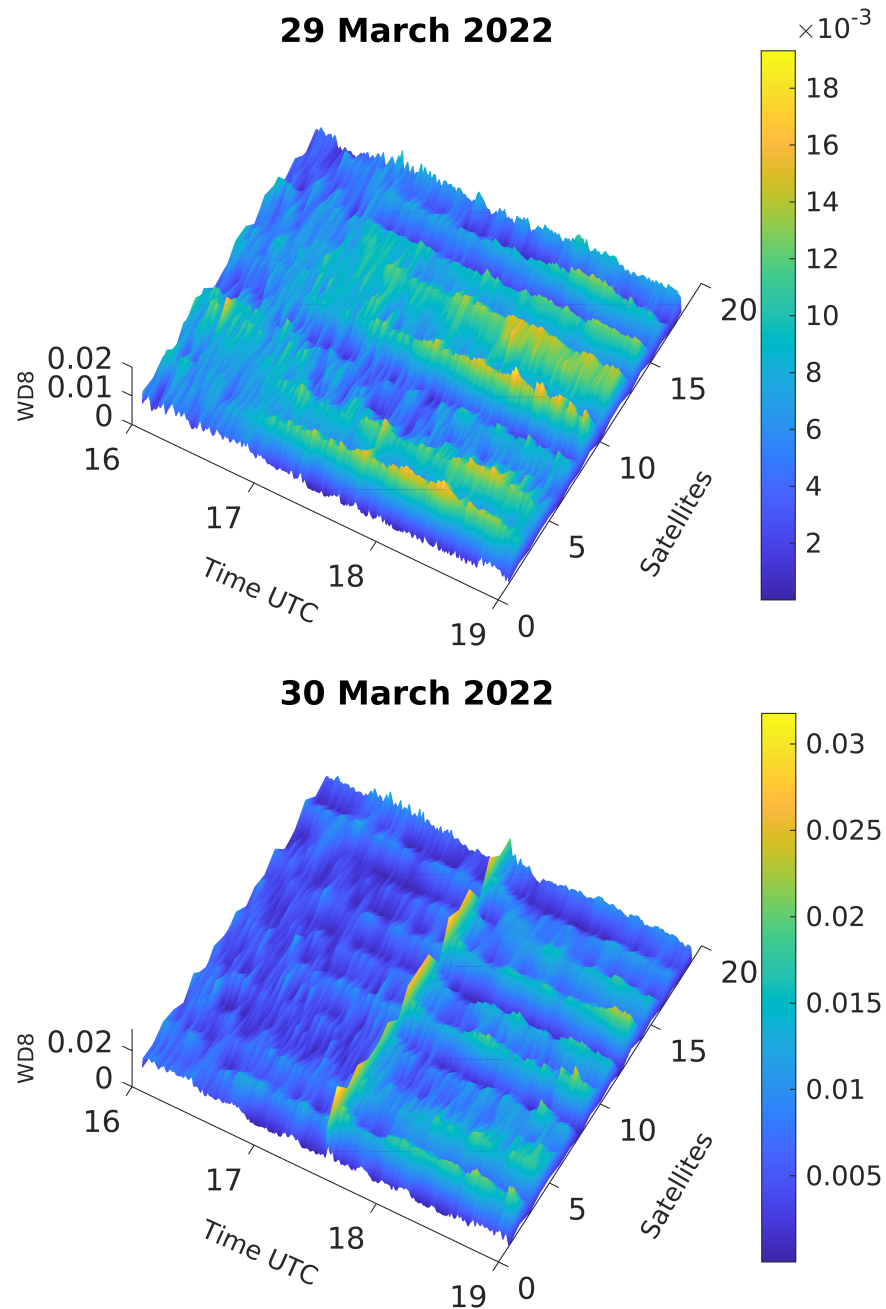


Figure 8. Visualization of Total Electron Content Wavelet Analysis from GNSS Signals for the Event on 30 March 2022.

3.4. Event 4 (30 April 2022)

The event of 30 April 2022 occurred in the solar spot region AR12994, located on the solar disk at N19 W90. Despite being in this location, it is possible to analyze the impact of this flare on the Earth's ionosphere, which was generated at 13:37 UTC, reached its maximum at 13:47 UTC, and ended at 13:52 UTC. The results of this event show a considerable increase in the wavelets after the event (Figure 9). This is a visible pattern where the flare did not have much impact. In this case, it is mainly noticeable in satellite 4. Additionally, it is possible to appreciate that there is not as much impact for the SPIG station as in the others, because this station is further north. The same happened in the other case where the location of the flare on the solar disk was very close to the edge.

During this event, we observed more distinct patterns of the diurnal cycle during the calm day. As the ionosphere began to charge, frequencies that impact the wavelet results

were detected. Once the increase subsided, the wavelets also decreased. However, concerning the event detection, the day of the event was clearly and concisely distinguishable (Figure 9).

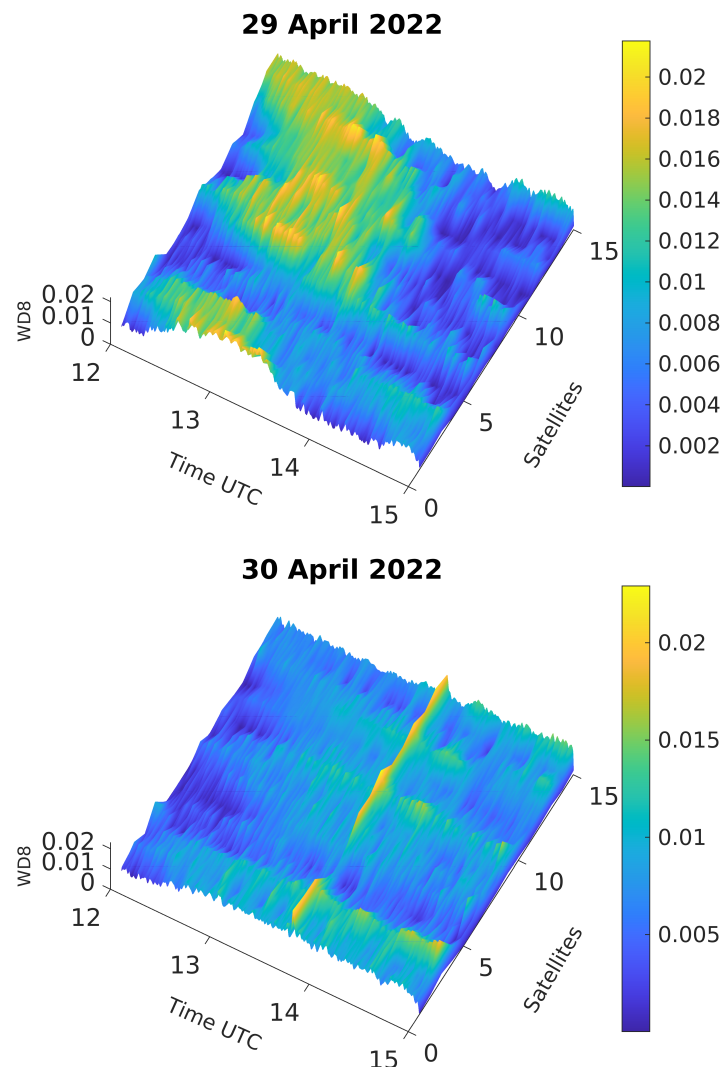


Figure 9. Visualization of Total Electron Content Wavelet Analysis from GNSS Signals for the Event on 30 April 2022.

3.5. Event 5 (10 May 2022)

On 10 May 2022, a solar flare of X1.5 type occurred in the AR13006 region located at S31 W10. The peak intensity was reached at 13:55 UTC, while the onset and end of the flare were recorded at 13:50 UTC and 13:59 UTC, respectively. During this event, all stations (UNPM, OXUM, SPIG, SSNX, and UCOE) experienced disturbances in the ionosphere, and the disturbances could also be observed in all satellites.

This event exhibited the most significant alterations in the wavelet results (Figure 10), displaying a pronounced disturbance with values nearing 0.05 at the level of detail 8. Considering that the average for the other events is around 0.02, this event experienced a more substantial alteration according to the wavelets. One possible reason for such pronounced disturbances in this event could be its solar flare's location on the solar disk, originating from the central part of the Sun. It is worth mentioning that, in the case of the calm day, we obtained maximum wavelet values less than 0.01, demonstrating the correlation between flare-induced disturbances and wavelet outcomes.

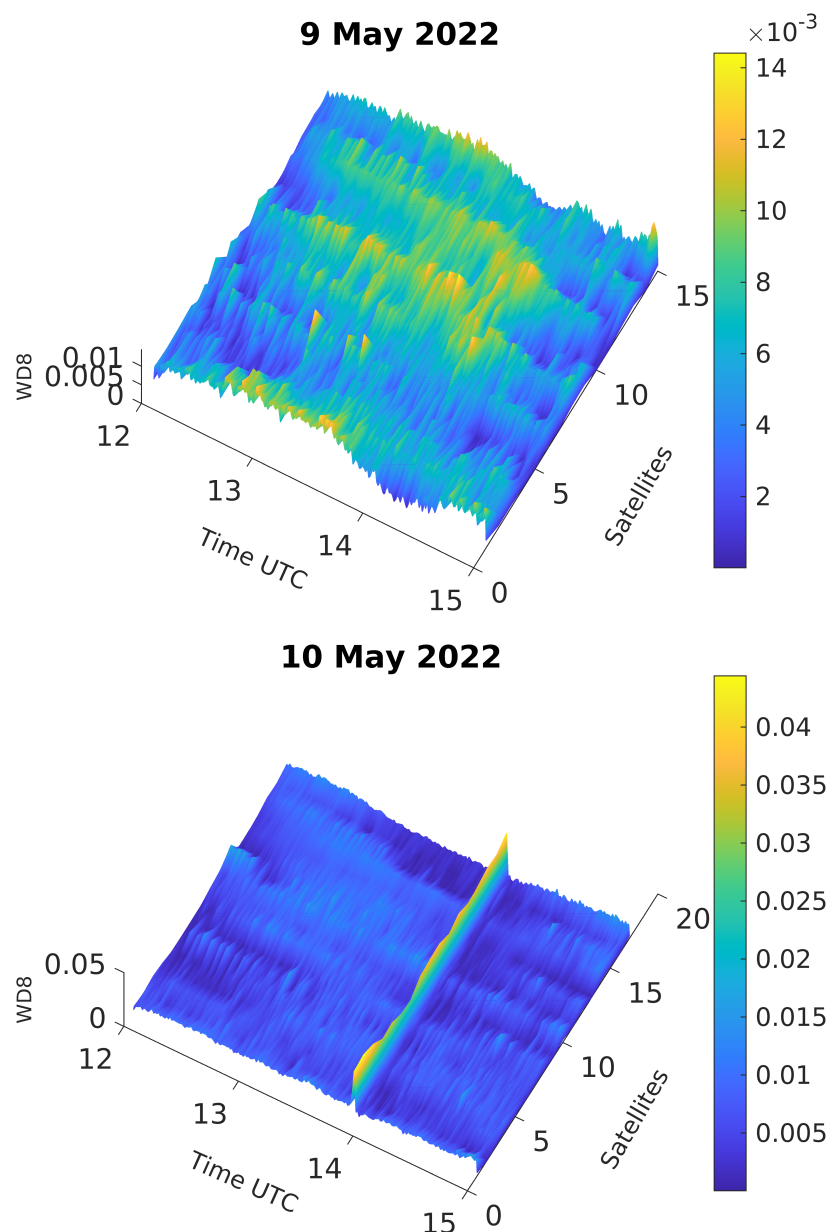


Figure 10. Visualization of Total Electron Content Wavelet Analysis from GNSS Signals for the Event on 10 May 2022.

3.6. Event 6 (2 October 2022)

The event of 2 October 2022 began at 19:53 UTC, reached its peak intensity at 20:25 UTC, and ended at 20:34 UTC. The genesis of this event can be traced back to the coordinates N16 W50, pinpointing the origin within the solar region AR13110. The impact of the solar flare on each of the satellites for all stations can be observed in the wavelet results. While some satellites show disturbances in the wavelets independent of the solar flare's impact, the maximum values of the wavelets occur precisely when the solar flare happens (see Figure 11).

The wavelet outcomes for this event revealed subtle alterations during the solar flare. Despite their subtlety, it was feasible to discern the moment when the flare impacted the ionosphere and distinguish between the results of a calm day and a day affected by the flare-induced disturbances (Figure 11).

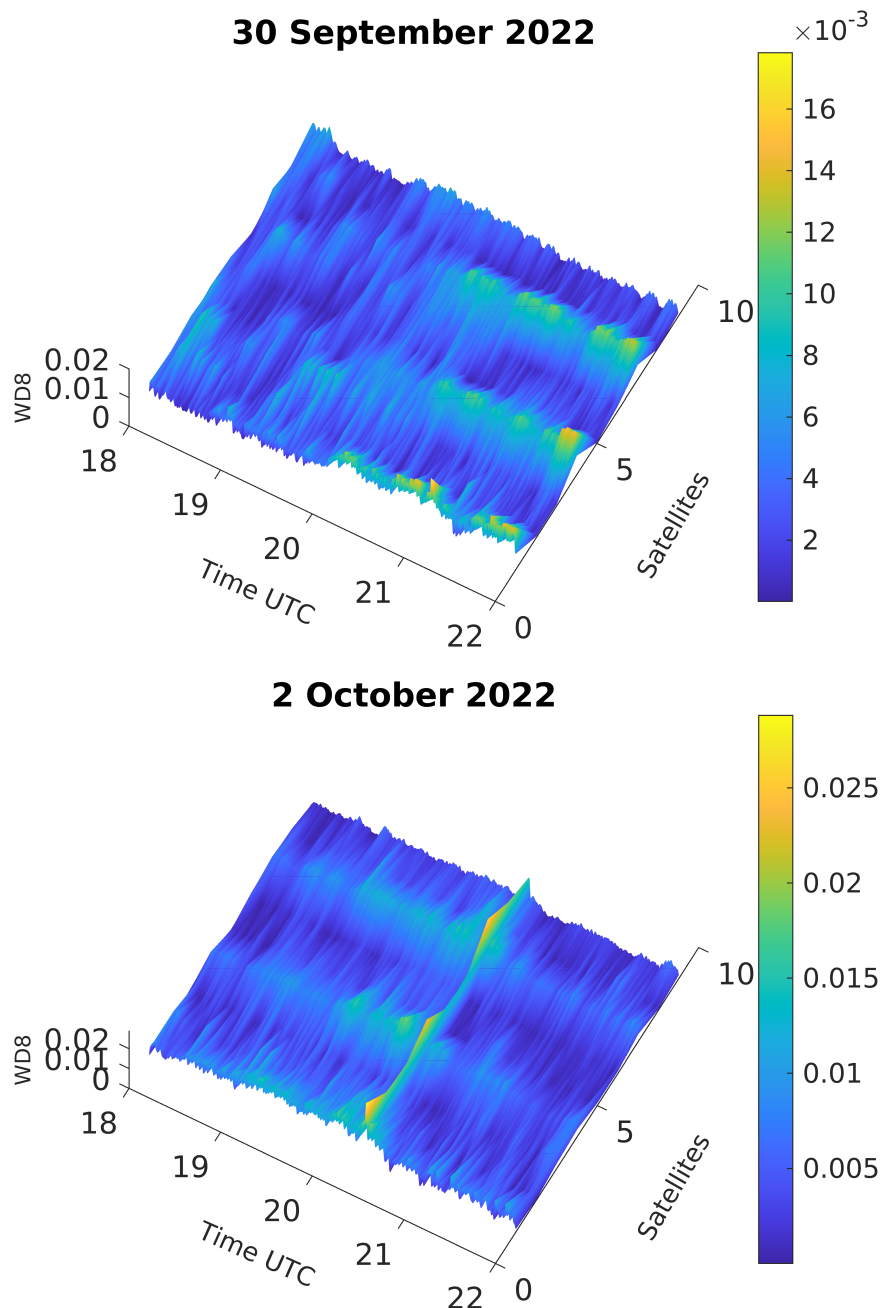


Figure 11. Visualization of Total Electron Content Wavelet Analysis from GNSS Signals for the Event on 2 October 2022.

Conducting the methodology’s implementation on days characterized by tranquil Total Electron Content (TEC) conditions, unaffected by storms or phenomena that atypically disrupt the TEC, is pivotal. This approach allows for the comparison of results between normal days and days influenced by solar flares, as seen in prior events. However, by conducting an aggregation of wavelet results for each station, a coherent and distinctive pattern emerges, revealing the solar flare’s consistent impact on the total electron content within the ionosphere. This visual representation is showcased in Figure 12, where the average wavelet trends per station are depicted. This illustration unmistakably underscores that all events exhibit a discernible surge in wavelet values across all the stations employed in the analysis.

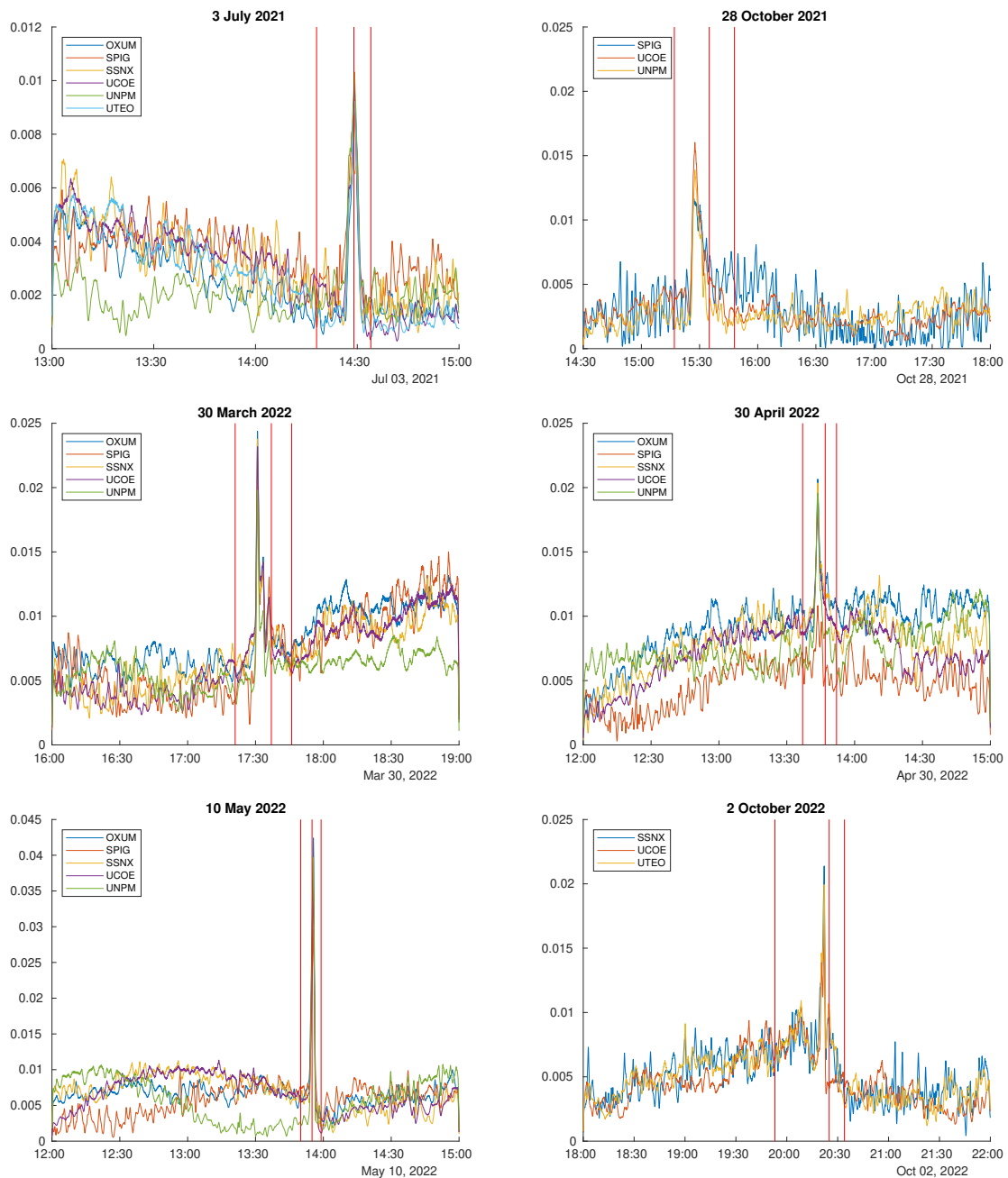


Figure 12. Averaging the wavelets per station of the analyzed events.

4. Conclusions

The comprehensive investigation into the interplay between solar flares and the ionosphere has yielded profound insights that hold vast implications for both scientific knowledge and practical applications. Through meticulous data analysis, strategic methodology selection, and rigorous validation, a nuanced understanding of the intricate relationship between these space weather events has emerged. A pivotal discovery arising from this study is the significant influence of sampling intervals on the detection and characterization of ionospheric disturbances induced by solar flares. The identification of previously unnoticed variations at high frequencies within the Total Electron Content (TEC) during solar flare events underscores the critical importance of selecting appropriate sampling intervals. The establishment of a 5 Hz sampling interval as optimal not only enhances the capture of sporadic events but also ensures efficient data processing. This choice was determined

through comprehensive testing, which demonstrated that higher sampling rates led to increased data volume without significantly improving event detection accuracy, while lower rates risked missing important fluctuations in TEC during solar flare events.

Furthermore, the implementation of wavelet analysis, particularly at levels 7 and 8, has provided unprecedented accuracy in portraying ionospheric perturbations caused by solar flares. This refined methodology, capable of detecting minute anomalies at 0.1 TECU and 2 Hz intervals, reaffirms its effectiveness in unraveling even subtle ionospheric fluctuations. The investigation reveals the influence of solar flares, specifically those of X-class intensity up to X2, on the ionosphere. Disturbances originating from solar flares even at the solar disk periphery emphasize the far-reaching consequences of these events. The convergence of anomalies across multiple monitoring stations solidifies their authenticity and establishes them as significant events with substantial implications for ionospheric dynamics. The study findings have been robustly validated through application to event-free days, confirming their accuracy and reliability. The alignment of detected perturbations with the onset and termination phases of solar flares further supports the causal link between solar flares and ionospheric disturbances, reinforcing the importance of these findings in the context of space weather phenomena.

In summary, this intricate study, involving thorough data analysis and accurate techniques, provides a novel approach for detecting solar influences on the ionosphere. While it represents an important step, further research is needed to deepen our comprehension of the complex interaction between solar flares and the ionosphere. Examining the ionosphere at these specific time points reveals certain frequencies that go unnoticed when investigating Total Electron Content (TEC) through individual stations and at lower frequencies.

Author Contributions: Conceptualization, C.L.-U. and G.E.V.-B.; methodology, C.L.-U. and K.N.; software, C.L.-U.; validation, C.L.-U., G.E.V.-B. and R.L.-M.; formal analysis, C.L.-U., R.L.-M. and K.N.; investigation, C.L.-U.; resources, C.L.-U. and K.N.; data curation, C.L.-U.; writing—original draft preparation, C.L.-U. and K.N.; writing—review and editing, C.L.-U. and K.N.; visualization, C.L.-U. and K.N.; supervision, G.E.V.-B. and R.L.-M. All authors have read and agreed to the published version of the manuscript.

Funding: This work was carried out with the support (CVU: 859540) of the National Council of Science and Technology (CONACyT) in Mexico.

Data Availability Statement: The data can be made available on request.

Acknowledgments: The authors would like to express sincere gratitude to the UNAM Geophysical Institute for their invaluable contribution to this research through the provision of essential data. The availability of this data was crucial in conducting a comprehensive analysis and achieving the outcomes presented in this manuscript. The authors also impart their deepest thanks to NASA for providing GOES satellite data. The authors further extend their heartfelt thanks to CONACyT (National Council for Science and Technology) for their financial support that made this research possible.

Conflicts of Interest: The authors declare no conflict of interest.

References

1. Budden, K.G. *The Propagation of Radio Waves: The Theory of Radio Waves of Low Power in the Ionosphere and Magnetosphere*; Cambridge University Press: Cambridge, UK, 1988.
2. Davies, K.; Smith, E.K. Ionospheric effects on satellite land mobile systems. *IEEE Antennas Propag. Mag.* **2002**, *44*, 24–31. [[CrossRef](#)]
3. Yuan, Y.; Tscherning, C.; Knudsen, P.; Xu, G.; Ou, J. The ionospheric eclipse factor method (IEFM) and its application to determining the ionospheric delay for GPS. *J. Geod.* **2008**, *82*, 1–8. [[CrossRef](#)]
4. Klobuchar, J.A. Ionospheric time-delay algorithm for single-frequency GPS users. *IEEE Trans. Aerosp. Electron. Syst.* **1987**, *AES-23*, 325–331. [[CrossRef](#)]
5. Prieto-Cerdeira, R.; Orús-Pérez, R.; Breeuwer, E.; Lucas-Rodríguez, R.; Falcone, M. Performance of the Galileo single-frequency ionospheric correction during in-orbit validation. *GPS World* **2014**, *25*, 53–58.
6. Yuan, Y.; Wang, N.; Li, Z.; Huo, X. The BeiDou global broadcast ionospheric delay correction model (BDGIM) and its preliminary performance evaluation results. *Navigation* **2019**, *66*, 55–69. [[CrossRef](#)]

7. Feng, J.; Zhang, Y.; Li, W.; Han, B.; Zhao, Z.; Zhang, T.; Huang, R. Analysis of ionospheric TEC response to solar and geomagnetic activities at different solar activity stages. *Adv. Space Res.* **2023**, *71*, 2225–2239. [[CrossRef](#)]
8. Bilitza, D.; McKinnell, L.A.; Reinisch, B.; Fuller-Rowell, T. The international reference ionosphere today and in the future. *J. Geod.* **2011**, *85*, 909–920. [[CrossRef](#)]
9. Bhuyan, P.; Borah, R.R. TEC derived from GPS network in India and comparison with the IRI. *Adv. Space Res.* **2007**, *39*, 830–840. [[CrossRef](#)]
10. Eastwood, J.; Biffis, E.; Hapgood, M.; Green, L.; Bisi, M.; Bentley, R.; Wicks, R.; McKinnell, L.A.; Gibbs, M.; Burnett, C. The economic impact of space weather: Where do we stand? *Risk Anal.* **2017**, *37*, 206–218. [[CrossRef](#)]
11. Baker, D.; Daly, E.; Daglis, I.; Kappenman, J.G.; Panasyuk, M. Effects of space weather on technology infrastructure. *Space Weather* **2004**, *2*. [[CrossRef](#)]
12. Nishimoto, S.; Watanabe, K.; Kawai, T.; Imada, S.; Kawate, T. Validation of computed extreme ultraviolet emission spectra during solar flares. *Earth Planets Space* **2021**, *73*, 79. [[CrossRef](#)]
13. Yasyukevich, Y.; Astafyeva, E.; Padokhin, A.; Ivanova, V.; Syrovatskii, S.; Podlesnyi, A. The 6 September 2017 X-class solar flares and their impacts on the ionosphere, GNSS, and HF radio wave propagation. *Space Weather* **2018**, *16*, 1013–1027. [[CrossRef](#)]
14. Sreeja, V. Impact and mitigation of space weather effects on GNSS receiver performance. *Geosci. Lett.* **2016**, *3*, 24. [[CrossRef](#)]
15. Yadav, S.; Sunda, S.; Sridharan, R. The impact of the 17 March 2015 St. Patrick's Day storm on the evolutionary pattern of equatorial ionization anomaly over the Indian longitudes using high-resolution spatiotemporal TEC maps: New insights. *Space Weather* **2016**, *14*, 786–801. [[CrossRef](#)]
16. Reddybattula, K.D.; Panda, S.K.; Sharma, S.K.; Singh, A.K.; Kurnala, K.; Haritha, C.S.; Wuyyuru, S. Anomaly effects of 6–10 September 2017 solar flares on ionospheric total electron content over Saudi Arabian low latitudes. *Acta Astronaut.* **2020**, *177*, 332–340. [[CrossRef](#)]
17. Yuan, Y.; Ou, J. Auto-covariance estimation of variable samples (ACEVS) and its application for monitoring random ionospheric disturbances using GPS. *J. Geod.* **2001**, *75*, 438–447. [[CrossRef](#)]
18. Olwendo, O.; Baki, P.; Mito, C.; Doherty, P. Characterization of ionospheric GPS Total Electron Content (GPS-TEC) in low latitude zone over the Kenyan region during a very low solar activity phase. *J. Atmos. Sol.-Terr. Phys.* **2012**, *84–85*, 52–61. [[CrossRef](#)]
19. Eftaxiadis, K.; Cervera, M.A.; Thomas, R.M. *A Global Positioning System Receiver for Monitoring Ionospheric Total Electron Content*; Technical Report; Defence Science and Technology Organisation: Canberra, Australia, 1999.
20. Turel, N.; Arikian, F. Probability density function estimation for characterizing hourly variability of ionospheric total electron content. *Radio Sci.* **2010**, *45*, 1–10. [[CrossRef](#)]
21. Sardon, E.; Rius, A.; Zarraoa, N. Estimación del contenido total de electrones en la ionosfera usando datos del Sistema de Posicionamiento Global. *Física Tierra* **1993**, *5*, 167–182.
22. Araujo-Pradere, E. GPS-derived total electron content response for the Bastille Day magnetic storm of 2000 at a low mid-latitude station. *Geofísica Int.* **2005**, *44*, 211–218. [[CrossRef](#)]
23. Rodríguez, M. Estudio de Perturbaciones Ionosféricas a Través del Contenido Total de Electrones en Europa Meridional. Ph.D. Thesis, Universidad Complutense de Madrid, Madrid, Spain, 2017.
24. Brunini, C.; Camilion, E.; Azpilicueta, F. Simulation study of the influence of the ionospheric layer height in the thin layer ionospheric model. *J. Geod.* **2011**, *85*, 637–645. [[CrossRef](#)]
25. Colom, R.J.; Gadea, R.; Sebastia, A.; Martinez, M.; Ballester, F.; Herrero, V. Implementación de la Transformada Wavelet Discreta 2D con filtros no separables. In Proceedings of the I Jornadas Sobre Computación Reconfigurable y Aplicaciones, Alicante, España, 19 September 2001.
26. Mallat, S. Multifrequency channel decompositions of images and wavelet models. *IEEE Trans. Acoust. Speech Signal Process.* **1989**, *37*, 2091–2110. [[CrossRef](#)]
27. Osorio Sánchez, A. Algoritmo Para Detección de Vibraciones Anormales en Maquinarias Utilizando la Transformada Wavelet. *Repos. Nac. Conacyt.* 2006. Available online: http://catarina.udlap.mx/u_dl_a/tales/documentos/meie/osorio_s_a (accessed on 21 August 2023).
28. Eparvier, F.G.; Crotser, D.; Jones, A.R.; McClintock, W.E.; Snow, M.; Woods, T.N. The extreme ultraviolet sensor (EUVS) for GOES-R. In Proceedings of the Solar Physics and Space Weather Instrumentation III, San Diego, CA, USA, 4–6 August 2009; Volume 7438, pp. 31–38.

Disclaimer/Publisher's Note: The statements, opinions and data contained in all publications are solely those of the individual author(s) and contributor(s) and not of MDPI and/or the editor(s). MDPI and/or the editor(s) disclaim responsibility for any injury to people or property resulting from any ideas, methods, instructions or products referred to in the content.